MDPI

Article

Effect of TiC Particle Size on Processing, Microstructure and Mechanical Properties of an Inconel 718/TiC Composite Material Made by Binder Jetting Additive Manufacturing

Vadim Sufiiarov *[iD], **Artem Borisov** [iD], **Anatoly Popovich and Danil Erutin**

Institute of Mechanical Engineering, Materials, and Transport, Peter the Great St. Petersburg Polytechnic University, 195251 St. Petersburg, Russia
* Correspondence: vadim.spbstu@yandex.ru

Abstract: In this paper, the effect of TiC particle size on the microstructure and mechanical properties of an Inconel 718/TiC composite material fabricated using binder jetting additive manufacturing was investigated. Vacuum sintering, hot isostatic pressing and heat treatment as post-processing were applied to the samples. The addition of 1 wt% micron-sized TiC to the Inconel 718 matrix resulted in a significant increase in strength and relative elongation during tensile tests at both room temperature and 700 °C. The distribution of micron-sized TiC particles in the matrix was uniform, and the MC phase precipitated after HT was located along the grain boundaries and near the micron-sized TiC particles, which contributed to the strengthening. The hardness increased insignificantly with the addition of micron-sized TiC. The nano-sized TiC particles added to the matrix were located on the surfaces of the Inconel 718 particles of the initial powders, which obstructed sintering and resulted in a porous structure and, consequently, low mechanical properties.

Keywords: additive manufacturing; binder jetting; Inconel 718; TiC; composite material; mechanical properties

1. Introduction

Inconel 718 is a nickel-based superalloy that is widely used for high-temperature applications such as turbine blades, turbocharger rotors and nuclear reactors because of excellent mechanical properties as well as oxidation and corrosion resistance [1–3].

Traditionally, Inconel 718 components are made by casting or forging. A feature of the microstructure of cast Inconel 718 is the segregation of alloying elements in the interdendritic regions and leads to the formation of an undesirable Laves phase, which requires multistage homogenization to dissolve [4]. Forged Inconel 718 also needs post-processing to remove macro-segregation, for example using vacuum arc remelting [5]. Thus, the cost of manufacturing products from Inconel 718 in the traditional way increases due to the need for post-processing, as well as the occurrence of scrap after machining [2].

The advantages of additive manufacturing are the possibility of producing parts with complex shapes that are difficult or impossible to produce by traditional methods, a significant reduction in the production time of the final part and a reduction in the formation of scrap. Many researchers have already studied in detail the process parameters, microstructure and mechanical properties when manufacturing products from powder Inconel 718 by methods of selective laser melting (SLM) [1,6–10], electron-beam melting (EBM) [11–14] and direct laser deposition (DLD) [15,16]. At the same time, binder jetting (BJ) technology, which is promising and has been popular for the past few years in the production of ceramic and metal products [17–19], is currently still not sufficiently studied [20].

In [2], three different Inconel 718 powders with average sizes of 7 μm, 21 μm and 70 μm were used for printing using the binder jetting method. The densification during sintering and microstructure of the produced samples were investigated. The analysis of

the chemical compositions showed some variation in the content of the individual alloy components with respect to each other in the powders considered. This, in turn, led to different solidus and liquidus values being calculated by the software. It was shown that the liquidus temperature of the alloy with an average size of 21 µm in the initial powder was 30 and 40 °C higher than the powders with sizes 7 µm and 70 µm, respectively. All samples were sintered at 1290 °C for 5 h. Density measurements showed that the samples made from 7 µm and 70 µm powders had a relative density of 99.9%; this was in contrast to the sample made from a powder with an average size of 21 µm, which had a relative density of only 92%. The incomplete densification is attributed to sluggish diffusion kinetics due to the small volume fraction of the liquid phase (3%) compared with the samples made from powders of sizes 7 µm (35%) and 70 µm (40%). Complete densification of the sample made from the powder with an average size of 21 µm was achieved when the sintering temperature was increased to 1330 °C. The microstructure of the samples made from 7 µm and 21 µm powders was characterized by the absence of δ and Laves phases in contrast to the sample made from powder with an average size of 70 µm. It should be noted that the binder saturation level was lower (70%) during printing with the 70 µm powder compared with the 7 µm and 21 µm powders (80%). The higher binder saturation resulted in more residual carbon after debinding, which contributed to the formation of the MC phase instead of the δ and Laves phases.

In [21], Inconel 718 superalloy powder with an average fraction of about 10–14 µm was used for printing by the binder jetting method. The relative density of sintered samples also had a direct dependence on the sintering temperature. The highest relative density, equal to 95%, was achieved after sintering at 1260 °C with dwell time of 3 h. Tensile tests were carried out for sintered samples, as well as after complex heat treatment. In the sintered state, the specimens did not achieve the ASTM F3055-14 target values for ultimate strength and yield strength. This behavior is expected, since Inconel 718 is a dispersion-strengthening alloy and without additional heat treatment not enough precipitates are formed to harden the material. After heat treatment, the yield strength was higher than the previously stated standard and close in value to ASTM B637-18. The ultimate strength increased after heat treatment but still did not reach the values required by the standards.

Improving the mechanical properties of superalloys is an essential aspect of manufacturing parts operating at high temperatures. In addition to complex heat treatments that promote the formation of intermetallic compounds in the matrix, one of the ways to solve this issue could be the creation of metal matrix composites (MMCs) based on superalloys.

Carbide ceramics have the most advantageous properties in terms of their use as the strengthening phase in composites. The advantages are high melting point, high strength even at high temperatures, high wear and corrosion resistance, low density and a high chemical stability. Titanium carbide (TiC) is one of the most important metal carbides used in modern materials science. TiC has a high melting point (3067 °C), high Young's modulus (410–450 GPa) and high Vickers hardness (28–35 GPa) [22]. TiC has a NaCl-type cubic crystal lattice with a parameter of 4.33 Å [23]. Compared with titanium nitride (TiN), the addition of TiC as a strengthening phase in metal matrix composites results in higher sintered material density, higher strength characteristics and hardness [24].

Due to the increased risk of global warming in recent years, reducing CO_2 emissions is an especially important issue. A significant share of emissions comes from various kinds of transport, including cars. The most effective solution is to reduce the weight of cars by using new, stronger materials. This is why many researchers are devoting their work to the development of advanced third-generation high-strength steel (AHSS) [25]. The structure of these steels, such as Hardox 400 and Hardox 500, is martensitic with fine, regularly distributed, coherent carbides. Such a structure primarily increases yield strength, hardness and wear resistance [26]. In paper [25], the effect of the addition of TiC on the mechanical properties of the Fe–7%Mn alloy was investigated. The average crystallite size decreased when TiC was added to the alloy powders and the yield strength and hardness of the alloy were increased.

Infiltration and reactive sintering are the main types of technological processes for MMC manufacturing using binder jetting [27].

In paper [28], MMCs were obtained using a pressure infiltration process with an Inconel 718 melt of a porous ceramic billet made of TiC. The volume fraction of the strengthening phase was about 55%. The resulting composite material was 24% lighter than Inconel 718, and its hardness was almost 1.6 times higher that of Inconel 718. Tensile tests at room temperature showed a resulting ultimate strength of about 819 MPa, which is probably due to the high content of the strengthening phase. The infiltration technology itself implies a high-volume fraction of ceramics in the composite, which results in rather low values for tensile strength and relative elongation of the tested material. Thus, based on the characteristic mechanical properties and heterogeneous microstructure, this method cannot be used for particularly responsible applications [2].

In [29], MMCs were obtained by reactive sintering, namely due to in situ synthesis of carbides of alloying elements of Inconel 625 during sintering due to the use of a carbon-containing binder during printing by binder jetting. The sintering process conditions influenced phase composition, morphology and the distribution of carbides. When an inert atmosphere was used throughout the sintering process, the structure consisted of a nickel matrix core with NbC, Mo_2C and Cr_3C_2 phases and a shell consisting of Cr_3C_2. The use of a reducing atmosphere at the debinding stage led to the formation of a core structure without a shell of Cr_3C_2. The authors suggest that a change in the amount of carbon remaining after the debinding stage can be used to change the morphology and composition of the MMC; however, this method does not allow prediction of the exact quantitative ratio of the strengthening phase and the matrix metal and, consequently, the properties of the final MMC.

The authors of [30] describe the fabrication of an in situ synthesized MMC by hot pressing. Inconel 718 superalloy was used as a metal matrix to which 5 to 15 vol.% Ti_2AlC was added. Exposure to high temperature contributed to the formation of ultradispersed TiC particles evenly distributed in the matrix. The composite made with the addition of 5 vol.% Ti_2AlC had the best properties. At room temperature the ultimate strength of the MMC was 1410 MPa. At 700 °C the ultimate strength of the MMC was 1010 MPa, which was higher than the ultimate strength of the superalloy Inconel 718 by almost 15%.

Previously published papers have not investigated the effect of the particle size of the strengthening phase in the fabrication of Inconel 718 and TiC-based MMCs using binder jetting. In the present research, it was decided to fabricate an MMC by adding 1 wt% TiC to Inconel 718 superalloy matrix and investigate the effect of TiC particle size on the microstructure and mechanical properties of the received MMC at different temperatures. The studies were carried out for sintered billets as well as for samples after additional postprocessing by hot isostatic pressing (HIP) and heat treatment (HT).

2. Materials and Methods

Inconel 718 powders (MetcoAdd 718C, Oerlicon, Pfäffikon, Switzerland), micron-sized TiC (which consists of polyhedral particles with a mean size of 17.1 microns) and nano-sized TiC (representing agglomerations of spherical particles with a mean size of 60 nm) (Sigma-Aldrich, St. Louis, MO, USA) were used as initial materials in this study. The chemical composition of Inconel 718 powder is shown in Table 1 [31]. The particle morphologies of micron- and nano-sized TiC powders are shown in Figure 1.

Table 1. The chemical composition of Inconel 718 powder data from [31].

Elements	Cr	Fe	Nb/Ta	Mo	Ti	Al	Ni
wt%	18	18	5	3	1	0.6	Bal.
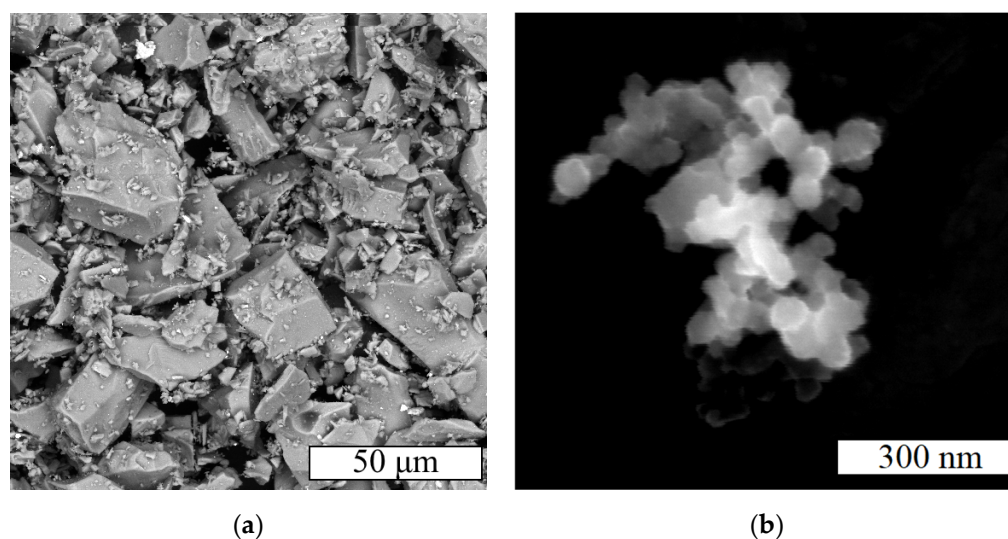
Figure 1. SEM images of powders: micron-sized TiC (**a**) and nano-sized TiC (**b**).

Powder mixtures of Inconel 718 and 1% TiC were prepared using a gravity mixer for 12 h.

The flowability of powders was determined using a Hall flowmeter. Determination of the apparent density of powders consisted of measuring the mass of the powder, which, in a free-flowing state, filled a container of known volume (25 cm^3).

To determine the particle size distribution of the powder, we applied a laser diffraction method using an Analysette 22 NanoTec plus analyzer (Fritsch GmbH, Idar-Oberstein, Germany) with a measuring range of 0.01–2000 μm.

The powder morphology and microstructure of the obtained samples were studied using a Tescan Mira3 LMU (Brno, Czech Republic) scanning electron microscope (SEM), as well as a Leica DMI5000 optical microscope (Leica Microsystems, Germany). A 1:3 mixture of HNO_3 and HCl with the addition of a drop of HF was used to etch the samples.

The samples were made using the ExOne Innovent binder jetting system (The ExOne Company, North Huntington, PA, USA).

Differential scanning calorimetry (DSC) was used to determine the solidus temperature of the Inconel 718 superalloy, which was necessary to select the sintering temperature.

Phase analysis was performed using a Bruker D8 Advance X-ray diffractometer (XRD) (Billerica, MA, USA) using Cu-Kα (1/4 1.5418 Å) irradiation.

Hot isostatic pressing (HIP) was applied at 1160 °C and 130 MPa for 3 h in an argon atmosphere. The heat treatment (HT) of the samples was an annealing at 1060 °C with a holding time of 1 h followed by air cooling and aging. The aging included heating to 760 °C and holding for 10 h, then cooling to 650 °C for 2 h and holding at 650 °C for 8 h followed by air cooling. A Phoenix V | tome | x M300 high-resolution industrial computer tomographic system (Waygate Technologies, Wunstorf, Germany) was used for the X-ray microtomography analysis (xCT) of the samples.

The densities of the sintered samples and the samples after HIP were determined by the Archimedes method in water with the addition of a surfactant.

The hardness of the samples was determined using a Zwick/Roell Zhu hardness tester (Zwick Roell GmbH & Co., Ulm, Germany) using the Vickers method.

Tensile tests to determine the ultimate strength, yield strength and relative elongation were performed using Zwick/Roell z100 testing machines at room temperature and Zwick/Roell z050 at 700 °C (ZwickRoell GmbH & Co., Ulm, Germany).

3. Results

This section presents the results of a study of the technological properties and particle size distributions of the initial powders; the results of a study of the manufacturing process

of samples using binder jetting technology; the results of a study of the sintering process and the effect of its mode on the density of the samples; the results of a study of the effect of post-processing in the form of HIP and HT on the porosity and TiC particle distributions as well as on the microstructures of the samples; and the results of hardness measurements and tensile tests at room and elevated temperature.

3.1. Initial Powders

The initial powder Inconel 718 and its mixtures with micron-sized TiC and nano-sized TiC were investigated. The designations for the investigated powders are presented in Table 2.

Table 2. Designations for the investigated powders.

Powder	Designation
Inconel 718	INC
Inconel 718 + 1% micron-sized TiC	INC-m
Inconel 718 + 1% nano-sized TiC	INC-n
Inconel 718 + 0.5% micron-sized TiC + 0.5% nano-sized TiC	INC-mn

SEM images of the powders show that the shape of Inconel 718 particles can be characterized as round or spherical (Figure 2a) and the shape of micron-sized TiC particles can be characterized as polyhedral (Figure 2b), whereas they are evenly distributed among Inconel 718 particles. The nanoparticles of TiC are concentrated on the surface of the Inconel 718 particles (Figure 2c,d).
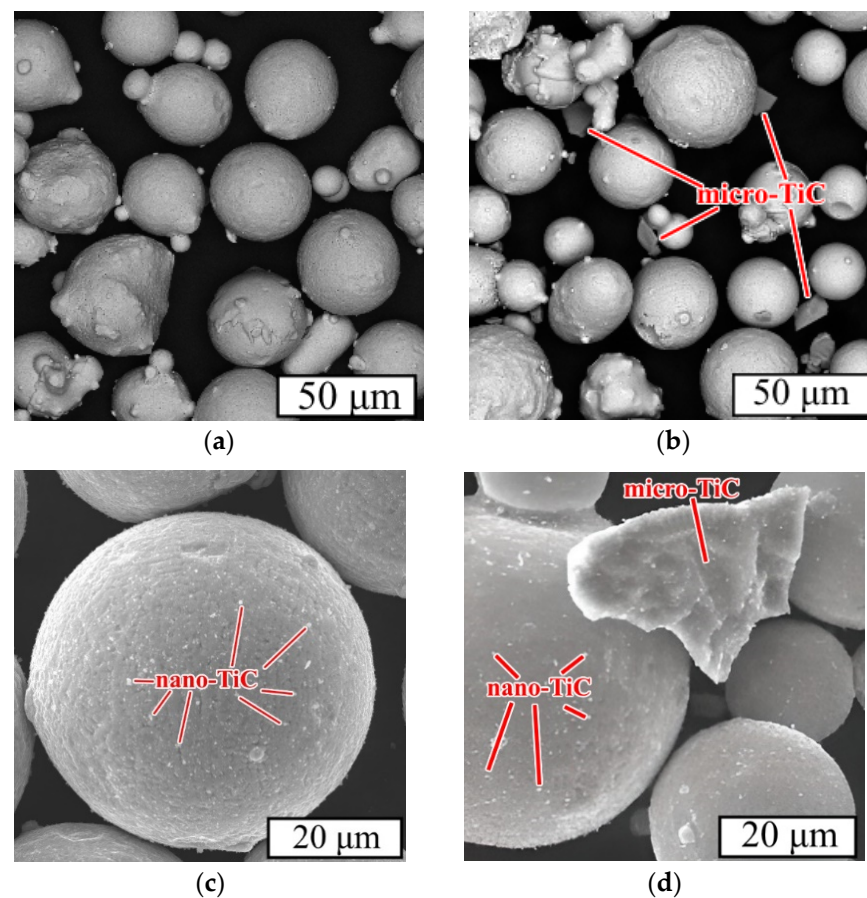
Figure 2. SEM images of the powders: INC (BSE) (**a**), INC-m (BSE) (**b**), INC-n (SE) (**c**) and INC-mn (SE) (**d**).

Table 3 shows the results of determining the technological properties of the powders. All the powders can freely pass through the Hall flowmeter, indicating their good flowability. The decrease in flowability and apparent density of the powders containing micron-sized TiC particles is probably related to the polyhedral morphology of these particles.

Table 3. Technological properties of the powders.

Powder	Flow Rate, s/50 g	Apparent Density, g/cm^3
INC	11.9 ± 0.1	4.40 ± 0.07
INC-m	13.6 ± 0.4	4.23 ± 0.05
INC-n	12.4 ± 0.2	4.35 ± 0.06
INC-mn	12.9 ± 0.3	4.31 ± 0.08

The data on the particle size distribution of the powders are presented in Table 4. The average particle sizes of all powders are similar in value and range from 38.5 to 39.8 μm.

Table 4. Particle size distribution of the powders.

Powder	d_{10}, μm	d_{50}, μm	d_{90}, μm
INC	21.4 ± 1.1	38.9 ± 1.1	66.4 ± 1.1
INC-m	21.6 ± 0.9	39.8 ± 0.9	68.3 ± 0.9
INC-n	22.7 ± 1.2	39.5 ± 1.2	69.4 ± 1.2
INC-mn	22.2 ± 1.0	38.5 ± 1.0	67.2 ± 1.0

3.2. 3D Printing of Green Models

Samples for the research were made using the binder jetting additive manufacturing process. Part of the samples had a cubic shape; the other part had a hexagonal prism shape. The parameters of the printing process of all samples were identical and are presented in Table 5.

Table 5. Parameters of the printing process.

| Parameter	Value
Layer thickness, mm	0.1
Saturation (%)	60
Bed Temp (°C)	27
Dry (s)	24

These values are similar to the printing parameters using Inconel 718 powder with binder jetting published in [2,32] and in aggregate, according to preliminary tests, are the most successful in terms of obtaining accurate geometry and density satisfactory for the green model.

The geometrically measured density of the green models as well as the theoretical density of the superalloy Inconel 718 [31] are presented in Table 6.

Table 6. Density values of green models and Inconel 718 superalloy.

Material	Density, g/cm^3
INC	4.67 ± 0.12
INC-m	4.39 ± 0.07
INC-n	4.65 ± 0.10
INC-mn	4.51 ± 0.10
Inconel 718	8.19

The images of the green models internal structures obtained by xCT are shown in Figure 3.
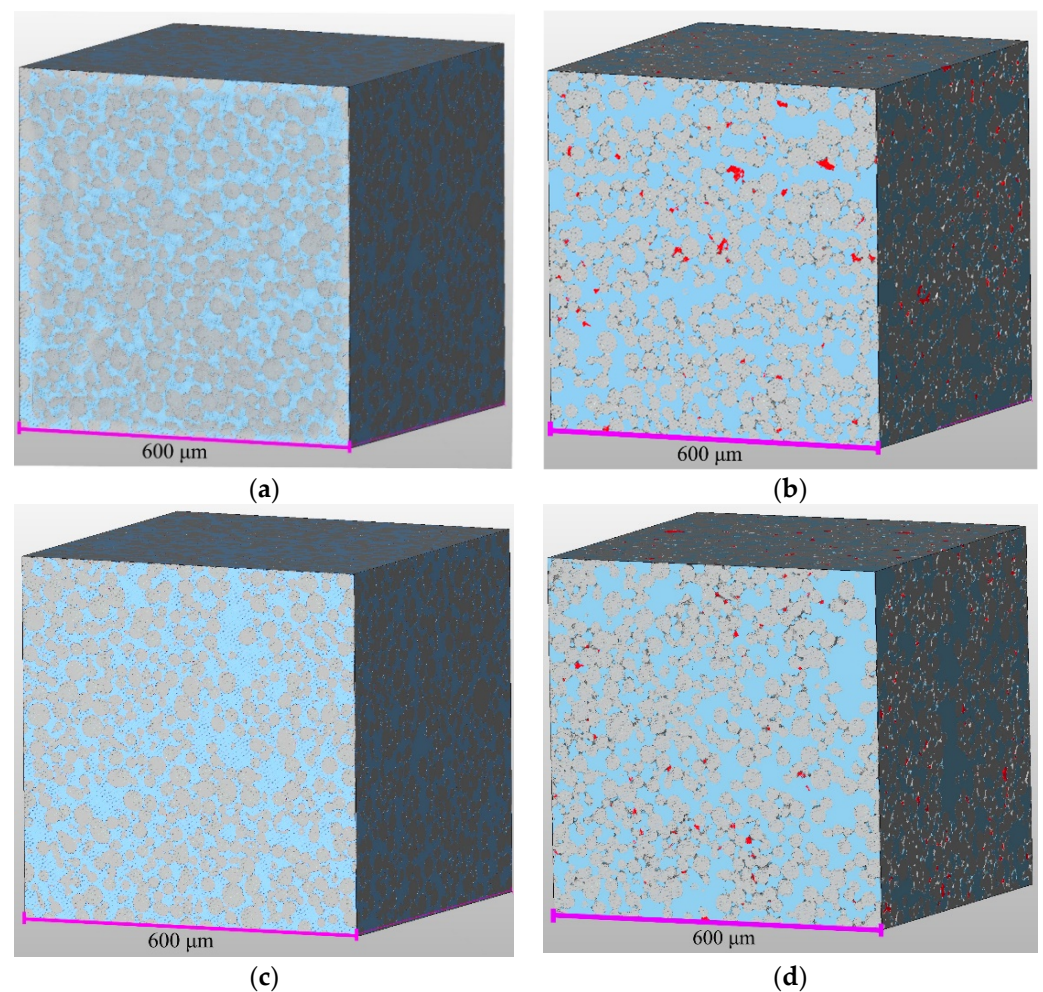
Figure 3. xCT images of green models, where Inconel 718 matrix is highlighted in gray, TiC particles are in red and pores are in blue: INC (**a**), INC-m (**b**), INC-n (**c**) and INC-mn (**d**).

Segmentation of the images into structural components demonstrates the distribution of micron-sized TiC particles. Sample INC-mn (Figure 3d) is characterized by fewer micron-sized TiC particles than sample INC-m (Figure 3b) because the initial powder of INC-mn contained half as many micron-sized TiC particles. The nano-sized TiC particles in the INC-n and INC-mn samples (Figure 3c,d) are not detected in these images.

3.3. Sintering of Samples

To determine the optimum sintering temperature for the INC powder, DSC analysis was carried out; the results are shown in Figure 4. The start and peak temperatures on the curve were considered as the solidus and liquidus, respectively. The solidus temperature obtained by DSC analysis was significantly higher than the solidus value specified by the manufacturer of the powder (1260 °C) [31].

Considering this fact, as well as the literature data on similar topics [2,32,33], the sintering processes of INC samples at temperatures of 1280 °C, 1290 °C, 1295 °C and 1300 °C in vacuum with dwell time of 5 h were carried out as preliminary tests. Each of the modes included a debinding stage at 600 °C for 1 h.

Images of the sintered samples are shown in Figure 5. The temperature of 1300 °C was probably too high, since the geometry of the sample changed significantly during sintering; therefore, no further studies for the sample sintered at this temperature were carried out. The sample sintered at 1295 °C also had some distortion of shape relative to its initial shape, namely, the widening of its lower part.
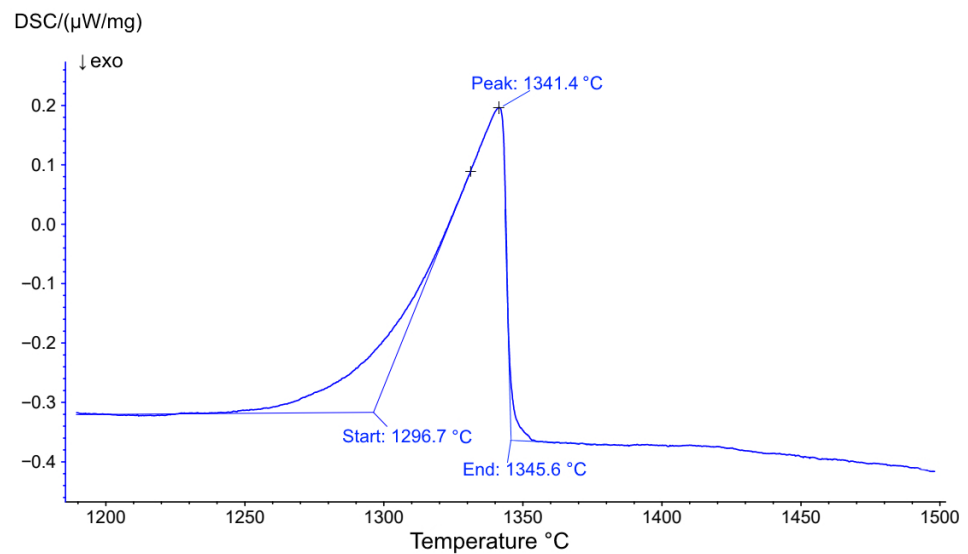
Figure 4. Result of the DSC analysis of INC.
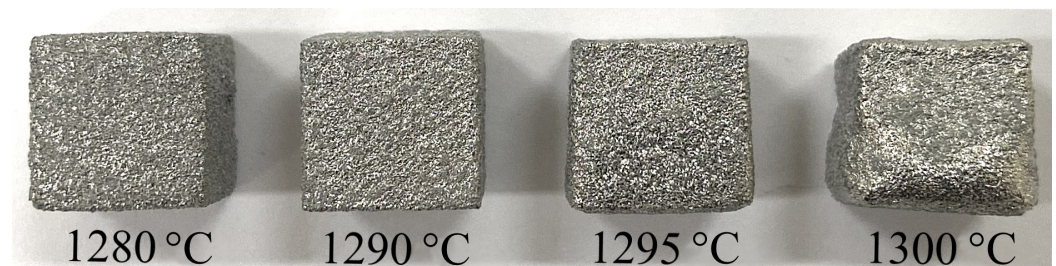
Figure 5. Image of INC samples sintered at different temperatures.

Samples sintered at temperatures of 1280 °C, 1290 °C and 1295 °C were investigated for porosity distribution. Optical microscopy images are shown in Figure 6. The sample sintered at 1280 °C (Figure 6a) is characterized by a relatively larger number of pores compared with samples sintered at temperatures of 1290 °C and 1295 °C (Figure 6b,c, respectively).

(**a**)   (**b**)   (**c**)
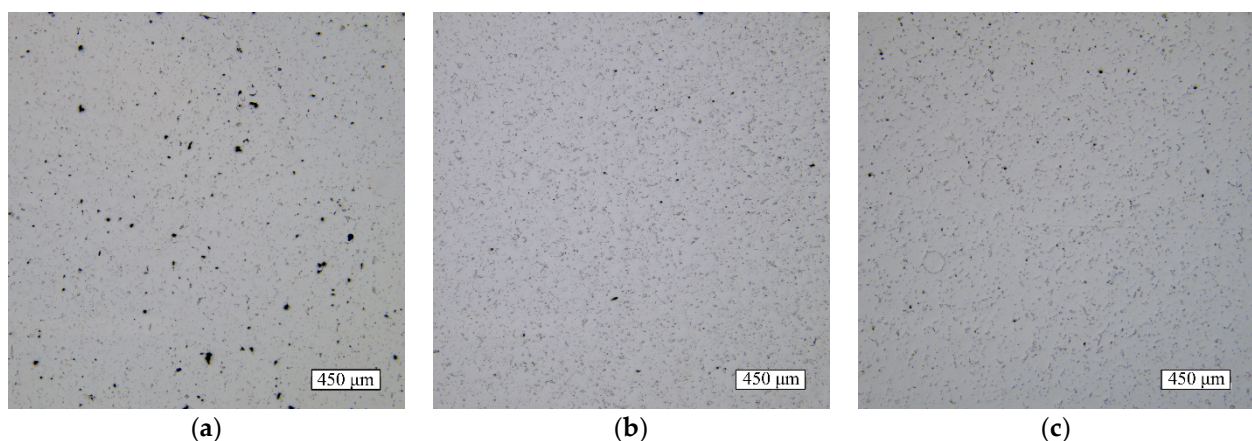
Figure 6. Images of cross sections with internal distribution of porosity in INC samples sintered at various temperatures: 1280 °C (**a**), 1290 °C (**b**) and 1295 °C (**c**).

The density of the samples was also measured. The results of the measurements are presented in Table 7. The highest density for the samples was obtained after sintering at 1295 °C, but, as described earlier, this sintering temperature was characterized by some distortion of the geometry of the samples. This is probably due to the proximity to the solidus temperature of the alloy, which was determined by DSC analysis.

Table 7. Density of INC samples sintered at different temperatures.

Sintering Temperature, °C	Density, g/cm^3
1280	7.61 ± 0.07
1290	7.96 ± 0.08
1295	8.04 ± 0.09

Thus, according to preliminary tests, the temperature of 1290 °C was determined as the optimum sintering temperature for INC in terms of density and preservation of the geometry of the samples. The final sintering mode used for all samples is shown in Figure 7.
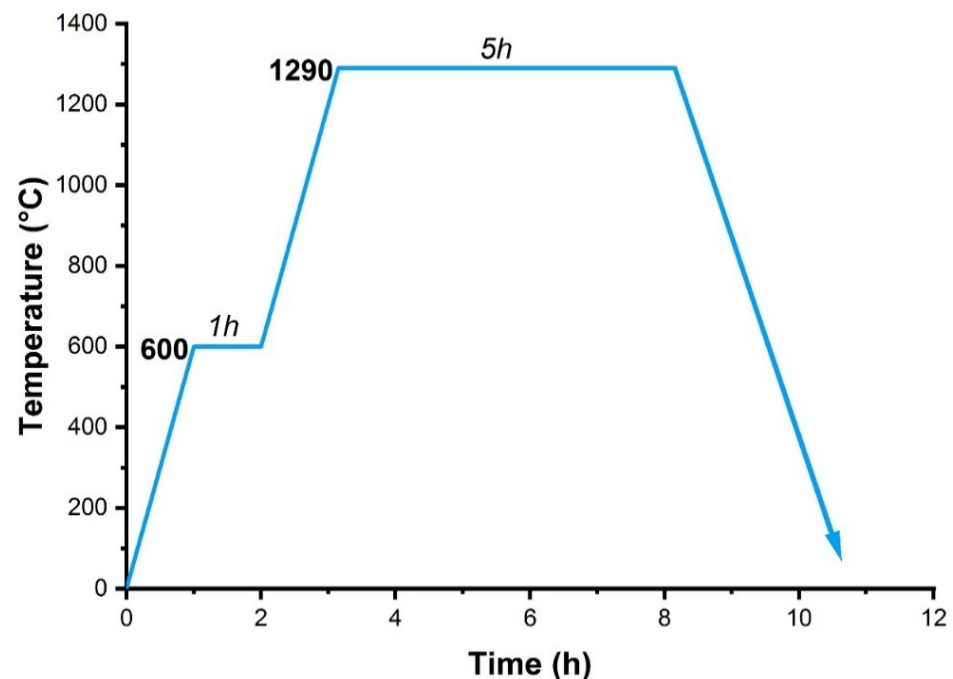
**Figure 7.** Thermogram of the sintering process.

3.4. Postprocessing, Microstructure Investigation and Mechanical Tests

The distributions of pores and TiC particles in the sample volumes after sintering was investigated using X-ray computed tomography and are shown in Figures 8 and 9, respectively. The greatest number of pores is observed in the INC-n sample. The distribution of TiC particles in all samples can be characterized as uniform.

Hot isostatic pressing was used as a post-treatment for the sintered samples. xCT images of the distributions of pores and TiC particles in the samples after HIP are shown in Figures 10 and 11, respectively. For the samples INC and INC-m, a significant decrease in the number and size of the pores is observed, which cannot be said about the samples INC-n and INC-mn containing nano-sized TiC. No noticeable change in the distribution of TiC particles after HIP treatment is observed.

Density was measured for the samples after sintering and HIP. The results are presented in Table 8.

The samples containing nano-sized TiC (INC-n and INC-mn) did not have a significant increase in density after HIP, which is consistent with the xCT data. This was probably due to the location of the nano-sized TiC particles on the surfaces of the Inconel 718 particles of the initial powder, which first prevented sintering and then additional densification during HIP.
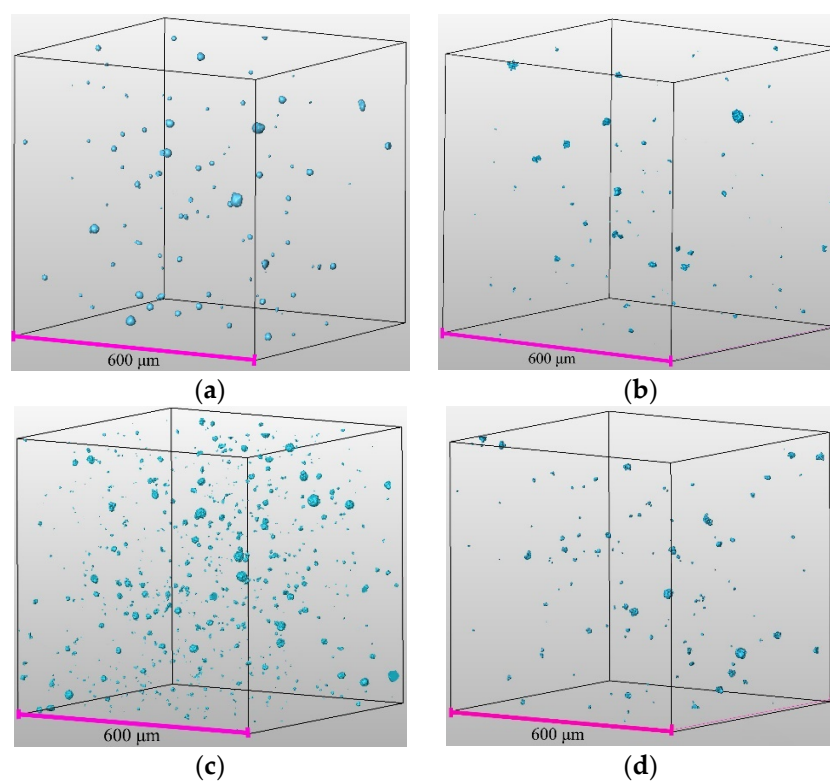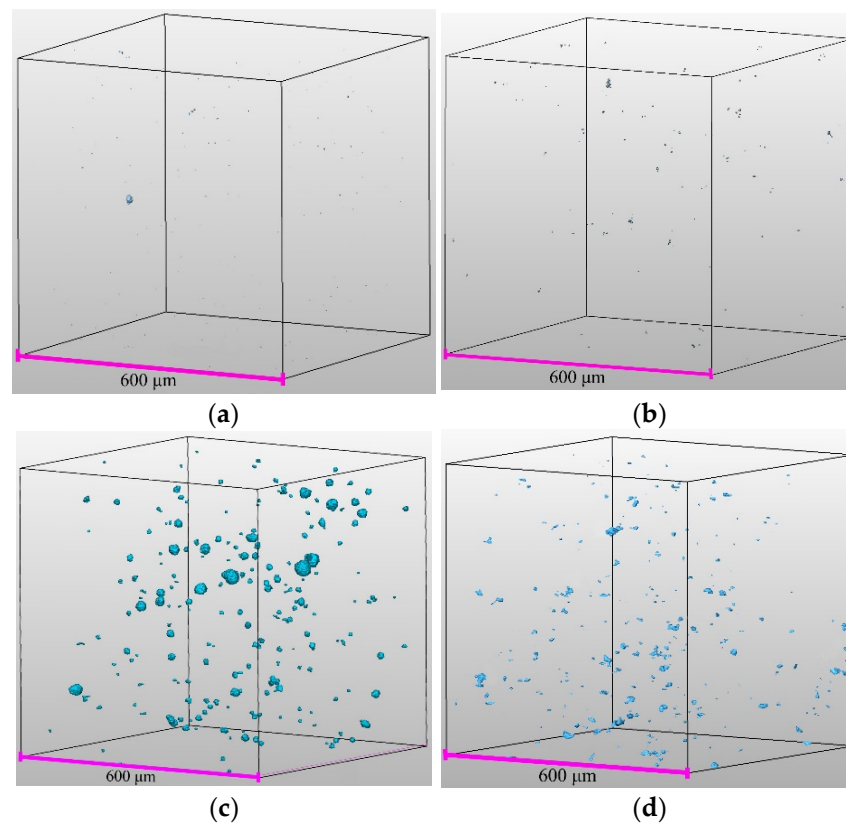
Figure 8. xCT images of pore distribution (highlighted in blue) in sintered samples: INC (**a**), INC-m (**b**), INC-n (**c**) and INC-mn (**d**).
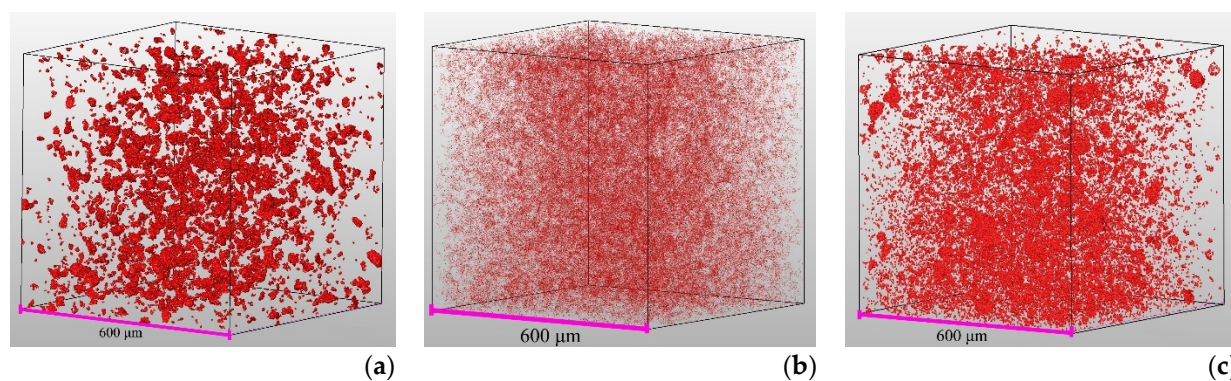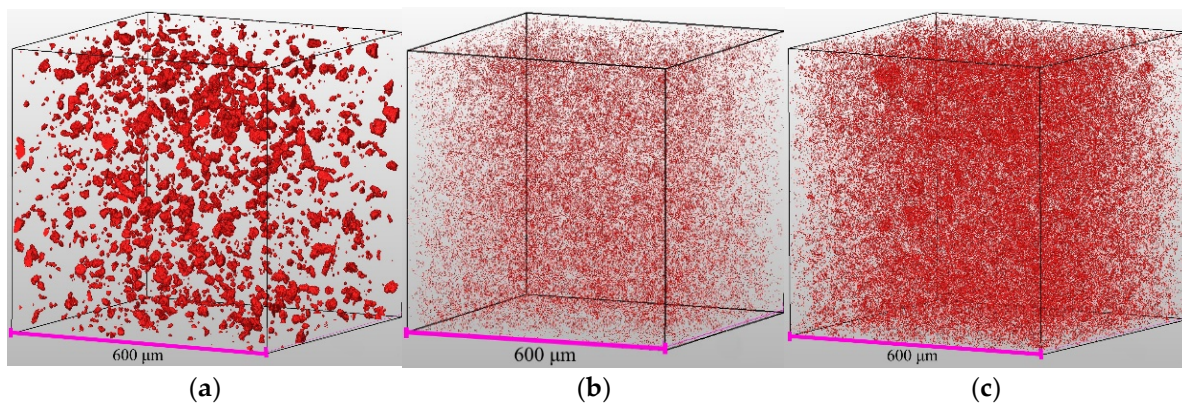

Figure 9. xCT images of TiC particle distribution (highlighted in red) in sintered samples: INC-m (**a**), INC-n (**b**) and INC-mn (**c**).

Table 8. Density of samples after sintering and HIP.

Sample	Density, g/cm^3	
	After Sintering	After HIP
INC	7.96 ± 0.08	8.17 ± 0.09
INC-m	7.94 ± 0.09	8.09 ± 0.08
INC-n	7.16 ± 0.06	7.21 ± 0.07
INC-mn	7.51 ± 0.07	7.58 ± 0.06

Figure 10. xCT images of pore distribution (highlighted in blue) in samples after HIP: INC (**a**), INC-m (**b**), INC-n (**c**) and INC-mn (**d**).

Figure 11. xCT images of TiC particle distribution (highlighted in red) in samples after HIP: INC-m (**a**), INC-n (**b**) and INC-mn (**c**).

Determination of the phase composition of the samples after the HIP and HT was carried out using X-ray diffraction. The XRD (Figure 12) demonstrates the presence of peaks at angles characteristic of γ and γ'' phases (the γ'' phase is coherent with the γ-phase, so their reflections are characterized by locations at the same angles). TiC is not defined by individual peaks distinguishable from the background, which is probably due to its small mass fraction (1 wt%).
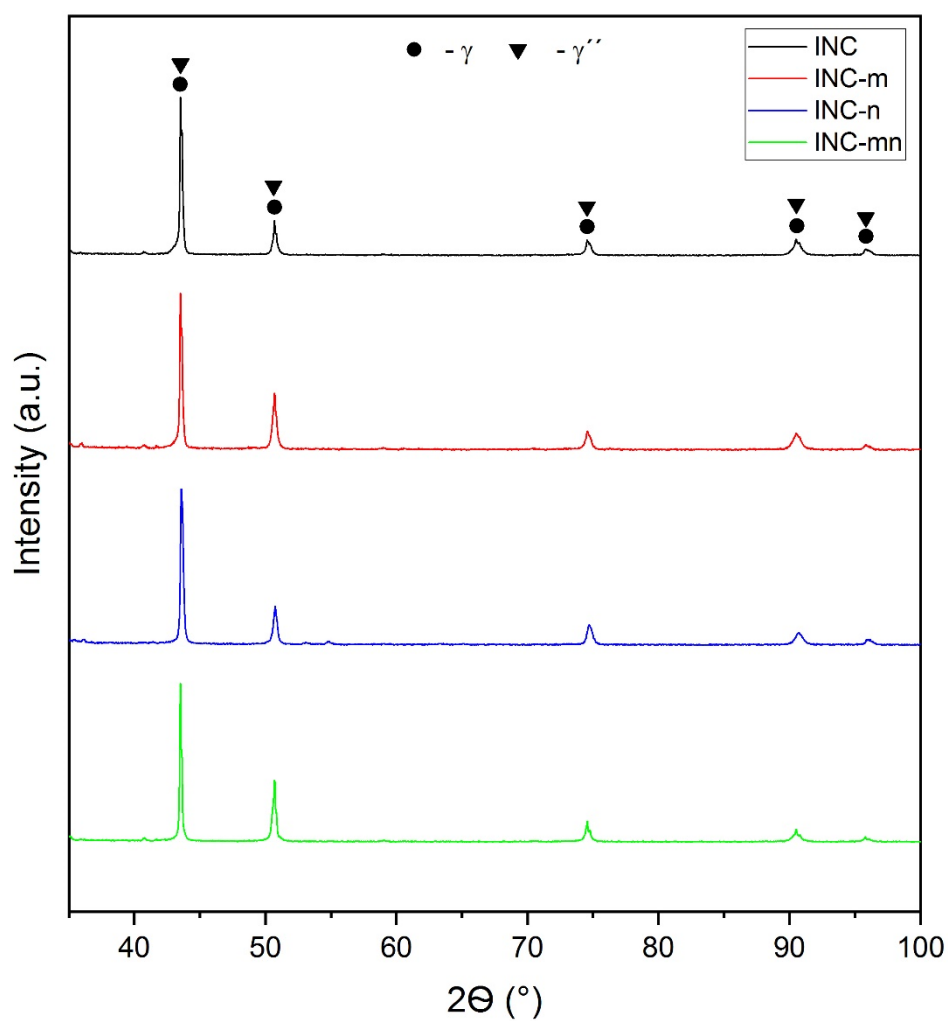
Figure 12. XRD of the samples after the HIP and HT.

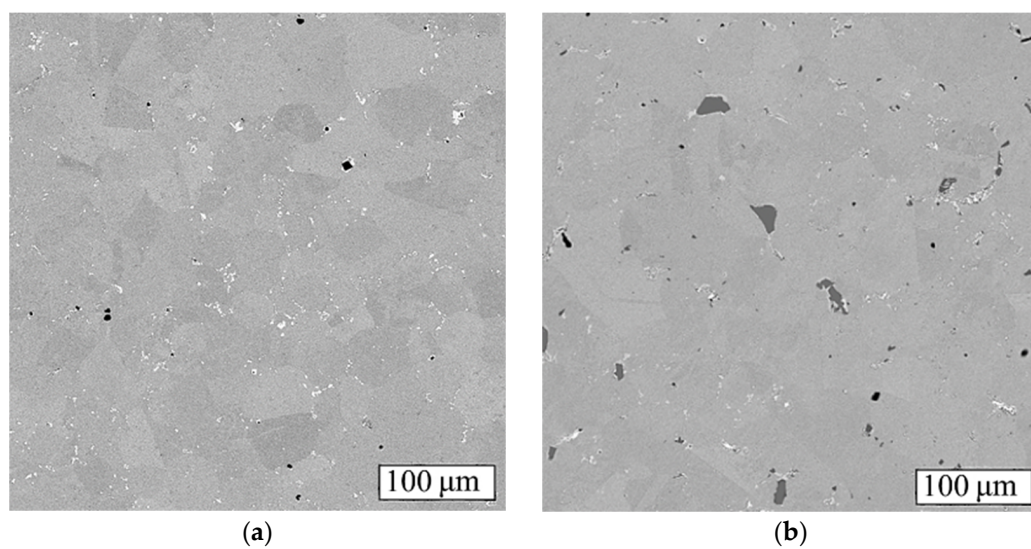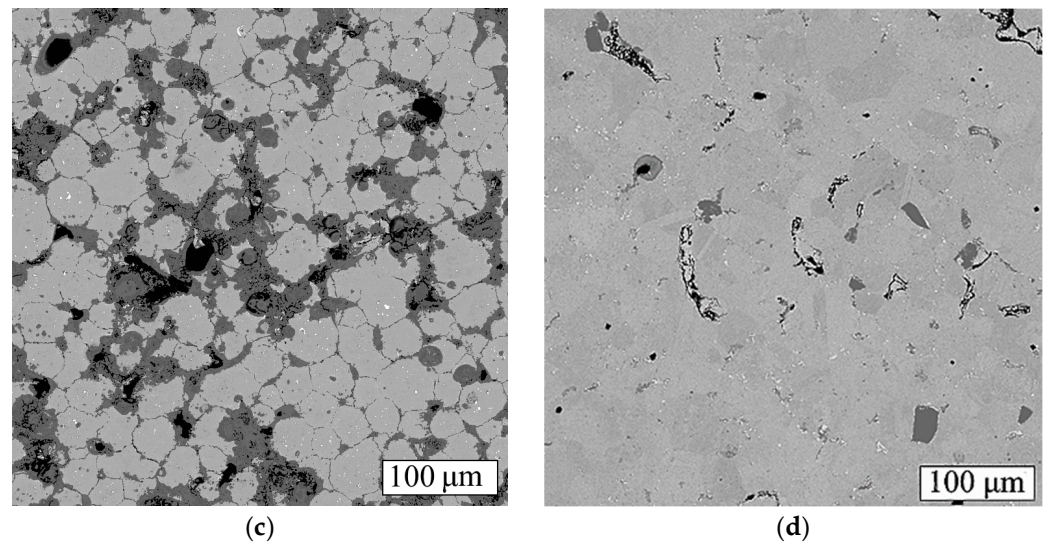The study of the microstructure was carried out using SEM, the results are shown in Figure 13.

Figure 13. *Cont*.

(**c**)   (**d**)

Figure 13. SEM images (BSE) of samples after HIP and HT: INC (**a**), INC-m (**b**), INC-n (**c**) and INC-mn (**d**). The black areas are pores and the dark gray areas are clusters of nano-sized TiC and micron-sized TiC particles.

The observed carbide phases (white in color) precipitated as a result of HT are complex carbides of the (Nb,Ta)C type [2], have an average size of about 0.5 µm and are located mainly at the grain boundaries in the INC, INC-m and INC-mn samples (Figure 13a,b,d), as well as near micron-sized TiC particles (Figure 14). In the INC-n sample (Figure 13c), this phase is located inside the grains and clusters of nano-sized TiC particles are observed along the grain boundaries.
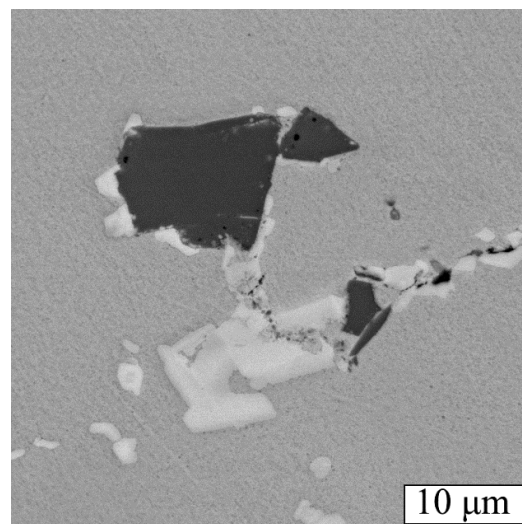
Figure 14. Precipitated carbide phase in the vicinity of micron-sized TiC particles.

Hardness measurements were carried out for sintered samples, as well as for samples after HIP and HT. The results of the measurements are presented in Table 9.

The addition of 1% micron-sized TiC to the Inconel 718 matrix (in the INC-m sample) resulted in a slight increase in hardness (about 8%) in the sintered state. Samples containing nano-sized TiC (INC-n and INC-mn) in the sintered state showed significantly lower hardness relative to the INC. The low hardness values for these samples are probably due to the high pore content in the samples, as evidenced by xCT data and the density measurements of the samples. HIP and HT resulted in an increase in hardness in all samples; however, the INC-n and INC-mn samples still had a lower hardness than the

others. The INC-m sample had a slightly higher hardness than the INC sample. The increase in hardness due to the addition of carbide particles into the metal matrix is associated with the obstruction of dislocation movement by solid particles, which contributes to the appearance of elastic deformations and hardening of the material. Only a slight increase in hardness is probably due to the small proportion of added particles (1 wt%).

Table 9. Hardness of samples (HV_{10}).

Sample	After Sintering	After HIP and HT
INC	229 ± 7	411 ± 12
INC-m	251 ± 8	425 ± 13
INC-n	140 ± 4	216 ± 6
INC-mn	148 ± 5	364 ± 10

The tensile tests were carried out at room temperature and 700 °C. The tests results for the samples after HIP and HT are presented in Table 10.

Table 10. Tensile mechanical properties at different temperatures.

Sample	Test Temperature, °C	YS, MPa	UTS, MPa	δ, %
INC	25	836 ± 8	1014 ± 10	4.49 ± 0.05
INC-m	25	975 ± 10	1160 ± 12	13.01 ± 0.13
INC-n	25	268 ± 3	308 ± 3	0.53 ± 0.01
INC-mn	25	587 ± 6	695 ± 6	1.65 ± 0.02
INC	700	669 ± 7	715 ± 7	1.45 ± 0.01
INC-m	700	782 ± 9	845 ± 8	4.17 ± 0.08
INC-n	700	-	203 ± 2	0.00
INC-mn	700	-	356 ± 4	0.00

An increase in mechanical strength and relative elongation was observed with the addition of 1% micron-sized TiC (INC-m sample). Tests at room temperature showed a 16% increase in yield strength, a 14% increase in ultimate strength and a 2.9-times increase in relative elongation compared with the INC sample. The 700 °C test showed a 17% increase in yield strength, an 18% increase in ultimate strength and an almost 2.9-times increase in relative elongation compared with the INC sample. In the INC-m samples, the (Nb,Ta)C phase, precipitated after HT, in addition to grain boundaries, was also located near micron-sized TiC particles, which were favorable sites for diffusion of carbide-forming alloying elements. This contributed to a more uniform (Nb,Ta)C distribution in the material volume, which probably played a role in the hardening effect [34].

Tests of INC-n and INC-mn samples showed that the addition of nano-sized TiC to the matrix does not allow for good mechanical properties at both room temperature and at 700 °C. In addition, brittle fracture behavior was observed in tests at 700 °C. The reason for the unsatisfactory mechanical properties seems to be the location of nano-sized TiC particles on the surfaces of Inconel 718 particles in the initial powder, which prevented the sintering process and densification of the material. Therefore, the samples containing nano-sized TiC had many pores and, consequently, lower mechanical properties.

4. Discussion

In the study reported in [35], similar composites were produced using SLM technology. An increase in the mechanical strength and a decrease in the relative elongation were observed when both micron-sized TiC and nano-sized TiC were added to the Inconel 718 matrix. This effect was related to the Orowan strengthening mechanism based on the bending of dislocations between particles. Moreover, a reduction in particle size from the micron to nano size resulted in higher strength due to the prevention of dislocation movement. However, this fabrication technology was related to melting, which contributed

to the uniform distribution of nano-sized TiC particles in the matrix. The BJ described in this paper does not achieve such a uniform distribution of nano-sized TiC in the matrix. The formation of clusters of nano-sized TiC particles and high porosity were the reasons for the low mechanical properties of the samples made using the binder jetting process.

The increase in mechanical properties when micron-sized TiC particles were added to Inconel 718 indicates the possibility of improving the operational characteristics of parts made of Inconel 718 using this method of strengthening. The upward trend in strength and elongation in both room- and high-temperature tests suggests that this composite can be used in high-temperature applications such as turbine blades, turbocharger rotors, etc., while also increasing the operating time and reducing repair and replacement costs. Binder jetting technology has some limitations related to density sintered blanks, but these can be successfully eliminated by the use of HIP. Research into the amount of micron-sized TiC added to the matrix when making such composites by binder jetting, as well as the use of other HT modes, is certainly interesting in terms of further improving the mechanical characteristics of the composite material and will be investigated in future studies.

5. Conclusions

The particle size of the TiC had a significant effect on the microstructure and mechanical properties of the Inconel 718/TiC composite material fabricated using the binder jetting process.

The addition of 1 wt% micron-sized TiC significantly improved the mechanical properties of the material: room temperature tests showed a 16% increase in yield strength, a 14% increase in ultimate strength and a 2.9-times increase in relative elongation; tests at 700 °C showed a 17% increase in yield strength, an 18% increase in ultimate strength and a 2.9-times increase in relative elongation. The distribution of micron-sized TiC particles in the matrix was uniform, and the (Nb,Ta)C phase precipitated after HT was located along the grain boundaries and near the micron-sized TiC particles, which contributed to the strengthening. The hardness with the addition of the micron-sized TiC increased insignificantly.

The addition of nano-sized TiC particles resulted in low mechanical properties that did not reach the measured values in Inconel 718 samples without additions of TiC. The reason for this was probably the location of the nano-sized TiC particles on the surfaces of the Inconel 718 particles in the initial powders, which prevented sintering. Therefore, the microstructures of the samples with added nano-sized TiC were characterized by clusters of nano-sized TiC particles and porosity.

Author Contributions: Conceptualization, V.S.; methodology, V.S. and A.B.; software, A.B.; validation, V.S., A.B. and D.E.; formal analysis, A.B. and D.E.; investigation, A.B. and D.E.; resources, V.S. and A.P.; data curation, A.B.; writing—original draft preparation, D.E.; writing—review and editing, V.S. and A.B.; visualization, A.B.; supervision, V.S.; project administration, V.S.; funding acquisition, V.S. and A.P. All authors have read and agreed to the published version of the manuscript.

References

1. Jia, Q.; Gu, D. Selective laser melting additive manufacturing of Inconel 718 superalloy parts: Densification, microstructure and properties. *J. Alloys Compd.* **2014**, *585*, 713–721. [CrossRef]
2. Nandwana, P.; Elliott, A.M.; Siddel, D.; Merriman, A.; Peter, W.H.; Babu, S.S. Powder bed binder jet 3D printing of Inconel 718: Densification, microstructural evolution and challenges. *Curr. Opin. Solid State Mater. Sci.* **2017**, *21*, 207–218. [CrossRef]
3. Sufiiarov, V.S.; Popovich, A.A.; Borisov, E.V.; Polozov, I.A. Evolution of structure and properties of heatresistant nickel alloy after selective laser melting, hot isostatic pressing and heat treatment. *Tsvetnye Met.* **2017**, *1*, 77–82. [CrossRef]
4. Radavich, J.F. The Physical Metallurgy of Cast and Wrought Alloy 718. *Superalloy* **2012**, *718*, 229–240. [CrossRef]
5. Ganji, D.K.; Rajyalakshmi, G. Influence of Alloying Compositions on the Properties of Nickel-Based Superalloys: A Review. *Recent Adv. Mech. Eng. Sel. Proc. NCAME* **2020**, *653*, 537–555. [CrossRef]
6. Teng, Q.; Li, S.; Wei, Q.; Shi, Y. Investigation on the influence of heat treatment on Inconel 718 fabricated by selective laser melting: Microstructure and high temperature tensile property. *J. Manuf. Process.* **2021**, *61*, 35–45. [CrossRef]
7. Wang, Z.; Guan, K.; Gao, M.; Li, X.; Chen, X.; Zeng, X. The microstructure and mechanical properties of deposited-IN718 by selective laser melting. *J. Alloys Compd.* **2012**, *513*, 518–523. [CrossRef]
8. Chlebus, E.; Gruber, K.; Kuźnicka, B.; Kurzac, J.; Kurzynowski, T. Effect of heat treatment on the microstructure and mechanical properties of Inconel 718 processed by selective laser melting. *Mater. Sci. Eng. A* **2015**, *639*, 647–655. [CrossRef]
9. Sufiyarov, V.S.; Borisov, E.V.; Polozov, I.A.; Masailo, D.V. Control of structure formation in selective laser melting process. *Tsvetnye Met.* **2018**, *7*, 68–74. [CrossRef]
10. Popovich, A.A.; Sufiiarov, V.S.; Borisov, E.V.; Polozov, I.A.; Masaylo, D.V. Design and manufacturing of tailored microstructure with selective laser melting. *Mater. Phys. Mech.* **2018**, *38*, 1–10. [CrossRef]
11. Pollock, T.M.; Tin, S. Nickel-Based Superalloys for Advanced Turbine Engines: Chemistry, Microstructure, and Properties. *J. Propuls. Power* **2006**, *22*, 361–374. [CrossRef]
12. Kotzem, D.; Dumke, P.; Sepehri, P.; Tenkamp, J.; Walther, F. Effect of miniaturization and surface roughness on the mechanical properties of the electron beam melted superalloy Inconel 718. *Prog. Addit. Manuf.* **2020**, *5*, 267–276. [CrossRef]
13. Strondl, A.; Palm, M.; Gnauk, J.; Frommeyer, G. Microstructure and Mechanical Properties of Nickel Based Superalloy IN718 Produced by Rapid Prototyping with Electron Beam Melting (EBM). *Mater. Sci. Technol.* **2011**, *27*, 876–883. [CrossRef]
14. Kirka, M.M.; Unocic, K.A.; Raghavan, N.; Medina, F.; Dehoff, R.R.; Babu, S.S. Microstructure Development in Electron Beam-Melted Inconel 718 and Associated Tensile Properties. *JOM* **2016**, *68*, 1012–1020. [CrossRef]
15. Blackwell, P.L. The mechanical and microstructural characteristics of laser-deposited IN718. *J. Mater. Process. Technol.* **2005**, *170*, 240–246. [CrossRef]
16. Petrat, T.; Brunner-Schwer, C.; Graf, B.; Rethmeier, M. Microstructure of Inconel 718 parts with constant mass energy input manufactured with direct energy deposition. *Procedia Manuf.* **2019**, *36*, 256–266. [CrossRef]
17. Sufiiarov, V.; Kantyukov, A.; Popovich, A.; Sotov, A. Structure and properties of barium titanate lead-free piezoceramic manufactured by binder jetting process. *Materials* **2021**, *14*, 4419. [CrossRef]
18. Sufiiarov, V.; Kantyukov, A.; Popovich, A.; Sotov, A. Synthesis of Spherical Powder of Lead-Free BCZT Piezoceramics and Binder Jetting Additive Manufacturing of Triply Periodic Minimum Surface Lattice Structures. *Materials* **2022**, *15*, 6289. [CrossRef]
19. Sufiiarov, V.; Polozov, I.; Kantykov, A.; Khaidorov, A. Binder jetting additive manufacturing of 420 stainless steel: Densification during sintering and effect of heat treatment on microstructure and hardness. *Mater. Today Proc.* **2019**, *30*, 592–595. [CrossRef]
20. Li, M.; Du, W.; Elwany, A.; Pei, Z.; Ma, C. Metal binder jetting additive manufacturing: A literature review. *J. Manuf. Sci. Eng. Trans.* **2020**, *142*, 090801. [CrossRef]
21. Eriksson, T. Process Optimization and Characterization of Inconel 718 Manufactured by Metal Binder Jetting. Master's Thesis, Luleå University of Technology, Luleå, Sweden, 2021.
22. Li, R. Synthesis and Structure of a New Mixed Cuprate-Titanate: La2Sr4Cu2Ti2O13. *Mater. Res. Bull.* **1996**, *31*, 539–543. [CrossRef]
23. The Materials Project. Available online: https://Next-Gen.Materialsproject.Org/Materials/Mp-631?Formula=TiC (accessed on 1 July 2023).
24. Gülsoy, H.O.; Gunay, V.; Baykara, T. Influence of TiC, TiN and TiC (N) Additions on Sintering and Mechanical Properties of Injection Moulded Titanium Based Metal Matrix Composites. *Powder Metall.* **2015**, *58*, 30–35. [CrossRef]
25. Jeon, J.; Choi, S.; Seo, N.; Moon, Y.H.; Shon, I.J.; Lee, S.J. Effects of TiC Addition on Strain-Induced Martensite Transformation and Mechanical Properties of Nanocrystalline Fe-Mn Alloy Fabricated by Spark Plasma Sintering. *Arch. Metall. Mater.* **2020**, *65*, 1249–1254. [CrossRef]
26. Frydman, S.; Pękalski, G. Modern Low-Alloy Wear-Resistant Steels-Structure And Impact Strength. *Int. Sci. J. Mach. Technol. Mater.* **2010**, *4*, 45–46.
27. Srivatsan, T.S.; Harrigan, W.C., Jr.; Murph, S.H. *Metal-matrix Composites*; Springer Nature: Cham, Switzerland, 2021; pp. 65–74.
28. Cho, S.; Lee, Y.H.; Ko, S.; Park, H.; Lee, D.; Shin, S.; Lee, S.K. Microstructure and Properties of TiC-Inconel 718 Metal Matrix Composites Fabricated by Liquid Pressing Infiltration Process. *Compos. Res.* **2019**, *32*, 158–162. [CrossRef]
29. Enrique, D.; Mahmoodkhani, Y.; Marzbanrad, E.; Toyserkani, E.; Zhou, N.Y. In situ formation of metal matrix composites using binder jet additive manufacturing (3D printing). *Mater. Lett.* **2018**, *232*, 179–182. [CrossRef]
30. Hu, W.; Huang, Z.; Yu, Q.; Wang, Y.; Jiao, Y.; Lei, C.; Zhou, Y. Ti2AlC triggered in-situ ultrafine TiC / Inconel 718 composites: Microstructure and enhanced properties. *J. Mater. Sci. Technol.* **2020**, *51*, 70–78. [CrossRef]

31. Oerlikon Metco, MetcoAdd 718C. Available online: https://mymetco-europe.oerlikon.com/en-us/product/metcoadd718c (accessed on 5 July 2023).
32. Turker, M.; Godlinski, D.; Petzoldt, F. Effect of production parameters on the properties of IN 718 superalloy by three-dimensional printing. *Mater. Charact.* **2008**, *59*, 1728–1735. [CrossRef]
33. Sicre-Artalejo, J.; Petzoldt, F.; Campos, M.; Torralba, J.M. High-density inconel 718: Three-dimensional printing coupled with hot isostatic pressing. *Int. J. Powder Metall* **2008**, *44*, 35–43.
34. Luu, D.N.; Zhou, W.; Nai, S.M.L.; Yang, Y. Mitigation of solute segregation during solutionization of selective laser melted Inconel 718 through micron-TiC addition. *J. Alloys Compd.* **2022**, *897*, 163224. [CrossRef]
35. Sufiiarov, V.; Erutin, D.; Borisov, E.; Popovich, A. Selective Laser Melting of Inconel 718/TiC Composite: Effect of TiC Particle Size. *Metals* **2022**, *12*, 1729. [CrossRef]